Mechanical properties and elastic constants due to damage accumulation and amorphization in SiC

F. Gao* and W. J. Weber

Pacific Northwest National Laboratory, MS K8-93, P.O. Box 999, Richland, Washington 99352, USA
(Received 24 October 2003; revised manuscript received 2 February 2004; published 28 June 2004)

Damage accumulation due to cascade overlap, which was simulated previously, has been used to study the changes in elastic constants and the bulk and elastic moduli as a function of dose in SiC. These mechanical properties generally decrease with increasing dose, and the rapid decrease at low-dose levels indicates that point defects and small clusters play a more important role in the change in elastic constants than the topological disorder. The internal strain relaxations, which have no effect on the elastic constants, C_{11} and C_{12}, in a perfect SiC crystal, have a significant influence on the elastic constants calculated in damaged SiC. The elastic constants, C_{11}, C_{12}, and C_{44}, in the cascade-amorphized (CA) SiC decrease about 19%, 29%, and 46%, respectively. The bulk modulus decreases 23%, and the elastic modulus decreases 29%, which is consistent with experimental results. The stability of both the perfect SiC and CA-SiC under hydrostatic tension has been also investigated. The mechanical properties in the CA-SiC exhibit behavior similar to that in perfect SiC, but the critical stress at which the CA-SiC becomes structurally unstable is one order of magnitude smaller than that for perfect SiC.

I. INTRODUCTION

The excellent physical, chemical, and mechanical properties of silicon carbide (SiC) make it an attractive material for applications ranging from advanced electronic devices[1,2] to nuclear systems,[3,4] as well as for the space station.[5] Recent success in fabricating high-quality, single-crystal wafers and single-crystal epitaxial layers of SiC suitable for device production has stimulated worldwide activities in establishing technologies and device designs that make full use of this unique semiconductor. Ion-implantation doping and irradiation environments inevitably produce atomic-scale defects and lattice disorder in SiC. These defects not only affect virtually all electrical and optical properties of SiC, but also influence the performance of SiC-based electronic devices and structural components in harsh environments (e.g., high temperatures and high radiation). With the advent of more-sensitive microelectromechanical devices based on SiC, as well as the structural components used in nuclear reactors, the importance of accurate knowledge of the mechanical properties of component materials, particularly under irradiation, has grown. The evolution of microstructure under irradiation can lead to changes in the mechanical properties of SiC that will affect the performance of SiC-based electronic devices and nuclear components. Even small variations in temperature, stress state, and irradiation conditions can cause sufficient alteration of dimensional, elastic, and physical properties, which can be of concern. Consequently, several experiments have been carried out to study the dose dependence of mechanical properties in SiC irradiated with various ions[6,7] and neutrons.[8]

The changes in mechanical properties of single-crystal SiC due to ion-beam-induced amorphization have been estimated from measurements of surface and buried amorphous layers. In general, the hardness and elastic modulus in amorphized SiC are observed to decrease about 45% to 70% and 70% to 76%, respectively.[9,10] Specifically, Snead *et al.*[6] found that the elastic modulus in SiC, irradiated with carbon ions at low temperatures, decreased from 400 GPa in the unimplanted region to about 275 GPa in the amorphized region; whereas the hardness was observed to decrease from 41 to 32 GPa. Damage accumulation and the evolution of amorphous domains in single-crystal 6*H*-SiC irradiated with Ne$^+$, Ar$^+$, and Xe$^+$ ions have been studied, and the hardness and elastic modulus generally decrease with increasing dose, exhibiting a decrease of 47% and 24%, respectively, at the highest dose.[7] Furthermore, the mechanical properties of SiC amorphized by neutron irradiation[8] have also been investigated, and the results suggest a density decrease of 10.8% from the crystalline to amorphous state, a decrease in hardness from 38.7 to 21.0 Gpa, and a decrease in elastic modulus from 528 to 292 Gpa. Despite the considerable work carried out by several groups, there still exists significant uncertainty about the dose dependence of hardness and elastic modulus in SiC. In addition, it appears to be difficult to accurately determine the elastic constant changes as a function of dose in SiC. Not surprisingly, there is considerable interest in developing fundamental theoretical and computational models that are capable of describing the various physical properties of SiC as a function of microstructural change.

Molecular dynamics (MD) simulations have been previously used to study the accumulation of irradiation damage and the nature of the amorphization processes in 3*C*-SiC due to the overlap of 10 keV Si displacement cascades.[11,12] In these simulations, the damage state following each cascade was characterized and saved in a file for subsequent analysis of property changes. These cascade overlap results, together with the simulations of damage accumulation from low-energy recoils,[13] have provided significant insights into the mechanisms controlling the crystalline-to-amorphous (c-a) transformation and the relative importance of Frenkel pairs,

antisite defects, and defect clusters in the irradiation-induced amorphization of SiC. The results demonstrated that both Frenkel pairs and antisite defects play significant roles in the amorphization process and that the coalescence and growth of defect clusters is an important mechanism in the amorphization of SiC. The volume change due to cascade overlap exhibited two regimes of linear dependence on system energy and increased more rapidly with dose than either the system energy or the disorder, which indicated a significant contribution of isolated defects to swelling. In the present study, the elastic constants, bulk modulus, and elastic modulus are determined as a function of dose at 0 K, using the archived data files for the damage state following each cascade in 3*C*-SiC, which is the only cubic polytype and has a periodicity of stacking for the Si and C planes of three. The other polytypes show hexagonal and rhombohedral symmetry. For example, 6*H*-SiC is a hexagonal polytype where the periodicity of stacking is six. In addition, the lattice instabilities responding to isostatic stress under irradiation are also simulated in a perfect SiC crystal and in the cascade-amorphized (CA) SiC. It would have been of interest to obtain the finite-temperature behavior of elasticity in SiC; however, because of the large system used in the cascade overlap simulations, which would have made it difficult to converge the fluctuation terms, the finite-temperature elastic constants have not been determined. Also, considering the large number of cascade overlap events (140 cascades[11]), it would require considerable computational effort to get good statistics. On the other hand, the shift in elastic constants of SiC is only about 0.2% between 0 and 300 K;[14] thus, the trend of the changes in elastic constants, as well as that of the elastic and bulk moduli, as a function dose should essentially be captured by the present calculations.

II. COMPUTATIONAL METHOD

The computational methods employed to simulate cascade overlap and defect accumulation has been previously described in detail elsewhere;[11] thus, only the central principles are described in this paper. Molecular dynamics methods were employed to create and study cascade overlap events, with either constant volume or constant pressure, and periodic boundary conditions were imposed along three directions of the MD cell that contains 40 000 atoms ($10 \times 10 \times 50$ unit cells). A kinetic energy of 10 keV was given to an atom near the top of the MD cell to start the initial displacement cascade, which was then allowed to evolve for about 10 ps. The MD cell was further equilibrated for another 10 ps to maintain temperature control, with the atoms in the two boundary planes being coupled to a reservoir. The second and subsequent cascades were simulated with a similar procedure, but with random atoms and directions. A total of 140 displacement cascades were modeled to reach a completely amorphous state, and the accumulated dose following each cascade was given in MD displacements per atom (MD-dpa) to distinguish them from values reported in experimental studies.

The simulations of defect accumulation show that the dominant defects are single interstitials and monovacancies,
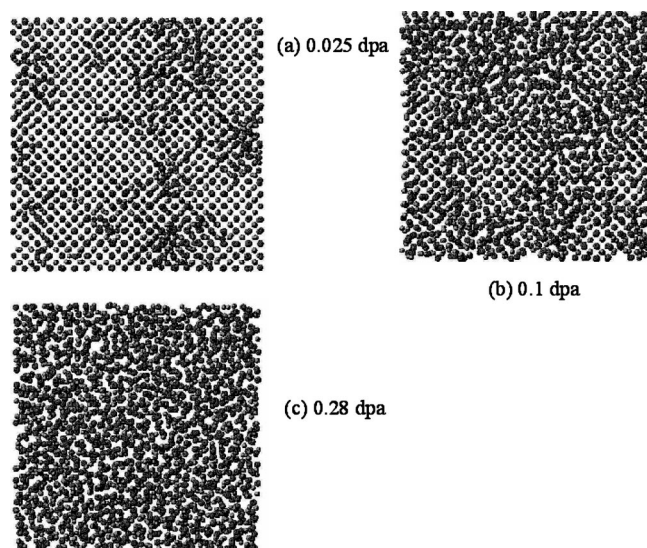

FIG. 1. Atomic plots showing defect accumulation, small cluster formation, and damage states at doses of (a) 0.025, (b) 0.1, and (c) 0.28 MD-dpa.

with some small clusters being created at low dose-levels within the cascades, as illustrated in Fig. 1(a). These small clusters contain two or three defects and are formed directly by collisions of energetic recoils. These clusters are similar to those found in a single cascade;[15] however, some clusters are dissociated during the cascade overlap process. The competition between creation and dissociation of small clusters represents a dynamic process for cluster formation during cascade overlap. The concentration of these clusters increases with increasing dose, and they are distributed randomly inside the MD cell. It has been observed that these small clusters can grow and coalesce to form disordered regions or amorphous domains during continued cascade overlap. Figure 1(b) shows a damage state at a dose of 0.1 MD-dpa, from which it can be seen that large disordered regions are formed at the original sites of the small clusters shown in Fig. 1(a). The increase in the number of clusters with increasing dose suggests that the formation of small clusters is a dominant process at low-dose levels, and the continued overlap of cascades stimulates the growth of the clusters into disordered regions at higher dose levels, giving rise to the formation of amorphous domains. A fully amorphous state is reached at a dose of about 0.28 MD-dpa, as shown in Fig. 1(c). At this dose, the long-range order is completely lost, but there exists a certain degree of local order and a partially correlated tetrahedral network. The amorphous character of the final structure at 0.28 MD-dpa is illustrated by the calculated pair-correlation function,[11] which is shown in Fig. 2 along with that obtained from the MD melt-quenched (MQ) amorphous sample. The contributions to the total pair-correlation function from Si-C, C-C and Si-Si pairs are presented separately. The pair-correlation function for the CA-SiC is generally similar to that of MQ-SiC amorphous sample, particularly in the positions and intensity of the peaks, which are consistent with a liquid-like structure without periodicity.

To study the changes of mechanical properties and elasticity in SiC, the set of 140 cascade overlap events and cor-
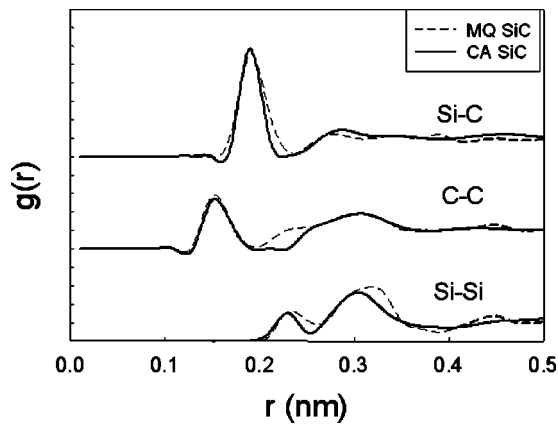
FIG. 2. Calculated pair correlation function, g, for cascade-amorphized (CA) SiC, along with the melt-quenched SiC for comparison, where the contributions from Si-C, C-C, and Si-Si pairs are shown separately.

responding damage states previously simulated[11] has been used. While it is recognized that more sets of cascade overlap events would improve statistics, the simulation of additional cascade sets would require considerable more computational efforts for each set. The purpose of the present study is to understand the basic physics and general behavior of the changes in mechanical properties and elastic constants as a function dose, rather than to obtain good statistics on these property changes. The archived MD cells representing the damage states after each cascade overlap event were further annealed at 200 K for about 50 ps under constant pressure conditions, and then quenched to 0 K. Computationally convenient strains, which are imposed along the MD cell axes, are defined as

$$\varepsilon_{ij} = \frac{1}{2}(e_{ij} + e_{ij}), \qquad (1)$$

where

$$e_{ij} = \frac{\partial u_i}{\partial x_j}, \qquad (2)$$

where u is the displacement and x is the positions of the atoms. A specific strain, aligned along a given axis, is imposed on the MD cell axis, and the elastic constants at 0 K are determined using a straightforward stress-strain relation defined by

$$C_{11} = \frac{\sigma_{xx}}{\varepsilon_{xx}}, \quad C_{12} = \frac{\sigma_{xx}}{\varepsilon_{yy}}, \quad C_{44} = \frac{\sigma_{yz}}{2\varepsilon_{yz}}, \qquad (3)$$

where σ_{ij} are the stress components. Furthermore, the bulk modulus can be also determined by imposing isotropic strains ($\varepsilon_{xx} = \varepsilon_{yy} = \varepsilon_{zz}$) and is given by:

$$B = V\frac{\partial^2 E}{\partial V^2}. \qquad (4)$$

In order to minimize the error in the calculations, particularly in the MD cells with high defect concentrations, all C_{ij} were calculated independently for all three orthogonal directions

and then averaged. In general, the variation of C_{11} and C_{12} is small, with typical values between 1% and 4%, but the variation of C_{44} is larger, and increased to 10% after a few overlapped cascades. Therefore, it is expected that C_{44} is less precise than C_{11} and C_{12}. Considering the large number of defects created in the computational cell, it is likely that some defects and defect clusters are formed in metastable configurations, and these defects will be relaxed to minimum energy states with respect to the isotropic and monoaxial expansion used to calculate C_{11}, C_{12}, and B. However, this may not be the case for the shear applied to calculate C_{44}. For the calculations of bulk modulus, fourth-order and fifth-order polynomial fits to the energy-volume curves were utilized, with higher-order fits being numerically unreliable. However, it should be noted that a simple relation among elastic constants can be used to calculate the bulk modulus for cubic materials, which is given by

$$B = \frac{C_{11} + 2C_{12}}{3}. \qquad (5)$$

Essentially, both methods give very similar results with an error of less than 0.7%. However, cubic symmetry does not strictly apply for the damage states created in SiC by cascade overlap, nor is the damaged SiC isotropic, except for the completely amorphous state. To compare with the experimental values of elastic modulus obtained in irradiated SiC, an averaged elastic modulus is calculated using the mean of the Reuss and Voigt averages.[16] The Reuss average of the elastic modulus, E_R, is related to polycrystalline materials without preferred orientation, which corresponds to orientational averages of the compliances. The Voigt average, E_V, is the average value of elastic stiffness over different orientations. The E_R and E_V values give the lower and upper bounds on the elastic modulus, and are defined by[17]

$$E_R = 5/(3S_{11} + 2S_{12} + S_{44}), \qquad (6)$$

$$E_V = \frac{(C_{11} - C_{12} + 3C_{44})(C_{11} + 2C_{12})}{2C_{11} + 3C_{12} + C_{44}}, \qquad (7)$$

where S_{ij} is the compliance tensor, which can be deduced using the elastic tensor C_{ij}.

For cascade overlap events, the interaction between atoms was described using Tersoff potentials along with a modification of short-range interactions based on ab initio calculations,[18] but the cutoff distances of the potentials were scaled by the cell volume for constant pressure conditions, as described by Tang and Yip.[19] The potentials have been employed to determine the threshold displacement energies in SiC, which are in good agreement with the results of first principles calculations and experimental methods.[20] The melting temperature of 3050 K determined from simulations based on these potentials is in reasonable agreement with the experimental value of 2800 K. Also, these potentials have been used to calculate defect properties,[21] and to study displacement cascades for recoil energies up to 50 keV in SiC.[22] These results, along with good descriptions of the equilibrium properties, such as the cohesive energy and elastic constants of perfect SiC and the accurate prediction of the shear
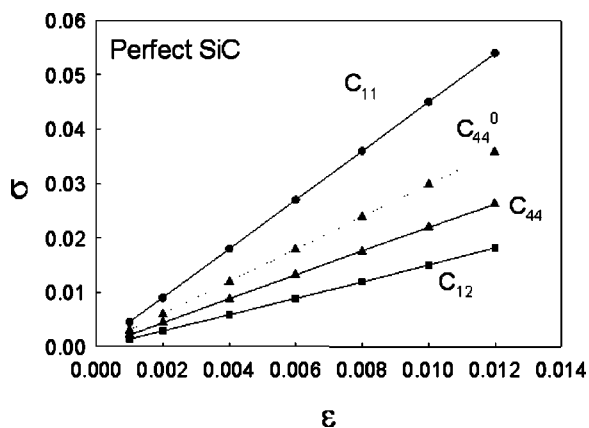
FIG. 3. Stress-strain curves for elastic constant calculations in a perfect SiC crysal, where the circles are data for C_{11}, squares for C_{12}, and triangles for C_{44} and C^0_{44}. The values for C^0_{44} are calculated without any internal relaxations.

elastic constant C_{44}, suggest that the potentials employed are well suited for the present investigation of mechanical changes due to defect accumulation and cascade overlap. However, it should be mentioned that these potentials can be applied to numerically calculate elastic constants and bulk modulus, but not for analytical analysis, because the second derivative of the cutoff function $f_c(r_{ij})$ is not continuous.

III. RESULTS AND DISCUSSION

A. Perfect SiC crystal

As a validation of the numerical approach, the elastic constants and bulk modulus in a perfect $3C$-SiC crystal are calculated and compared with those previously published based on similar Tersoff potentials. The results of the stress-strain curves at 0 K are shown in Fig. 3, where the dotted line represents the stress-strain relation without internal strain relaxation. The elastic constants are determined from the slopes of these curves, as indicated in Eq. (3). It is of interest to note that there are two shear elastic constants, namely C_{44} and C_{44}^0. While C_{44}^0 is the shear elastic constant without internal strain relaxation, C_{44} is the shear elastic constant with full internal strain relaxation and, thus, corresponds to the measured experimental values. In the present study, a specific strain is imposed on the MD cell, aligned along a given axis, and the internal strain is relaxed by MD simulations at 0 K, where the Si and C atoms move relative to each other by integrating the equations of motion until the forces on each atom vanish. The MD code is written specifically for calculation with the Gear 4-value predictor-correct algorithm in the N representation. The unrelaxed and relaxed values of C_{44} are 2.98 and 2.56 Mbar, respectively. For reasons of symmetry,[23] internal strain relaxation has no effect on C_{11} and C_{12}, as shown in Fig. 3, which is consistent with previous observations. The calculated values of the elastic constants, along with the bulk modulus and the elastic modulus, are summarized in Table I, together with experimental data and results obtained previously using similar potentials[19] for SiC. The present results give slightly larger values of C_{11} and

TABLE I. Comparison of $3C$-SiC properties obtained from the present work, a previous study using the similar Tersoff's potentials and experimental values. B is the bulk modulus, and E is the elastic modulus.

	Present work	Previous work (Ref. 19)	Expt.
C_{11}(GPa)	449	436	390[a]
C_{12}(GPa)	146	120	142[a]
C_{44}(GPa)	256	255	256[a]
B(GPa)	246	225	225[a]
E(GPa)	567	–	550[b]

[a]Reference 24.
[b]Reference 10.

B than the experimental values, but the equilibrium properties are generally consistent with the experimental data and previous studies. The Poisson ratio $\nu = -S_{12}/S_{11}$ is 0.23, which is in reasonable agreement with the experimental value of 0.26.[24] The excellent agreement of C_{12}, C_{44} and the elastic modulus, E, with the experimental results, as shown in Table I, suggests that the angular forces are satisfactorily characterized by the model potentials.

B. Elastic constants as a function of dose

To our knowledge, the shift in the elastic constants under irradiation has not been experimentally measured in SiC, but it is generally expected that the elastic constants decrease with increasing dose, particularly at high dose levels where the amorphous domains or large disordered regions are formed. As described above, the internal strain relaxation has no effect on the elastic constants, C_{11} and C_{12}, in a perfect SiC crystal, but it is found that the internal strain relaxation has a significant influence on all elastic constants calculated in the damaged SiC, particularly at high doses. This may be due to the fact that the point defects and defect clusters produced by the displacement cascades break the local symmetry in the crystal. To demonstrate this, the stress-strain curves at doses of 0.075 and 0.2 MD-dpa are shown in Figs. 4(a) and 4(b), respectively. Note that C_{11}^0, C_{12}^0, and C_{44}^0 are the elastic constants without the internal relaxation, as indicated by the dotted lines, whereas C_{11}, C_{12}, and C_{44} are those with full internal relaxation, as represented by the solid lines. In general, the internal strain relaxation affects all elastic constants calculated in the damaged SiC, with the largest effects on C_{44}, followed by C_{11} and C_{12}, respectively. Moreover, the internal strain relaxation decreases the values of C_{11} and C_{44}, but surprisingly increases the value of C_{12}, as shown in Fig. 4. For example, the decrease in C_{44} and C_{11} is about 51% and 32%, respectively, but the increase in C_{12} is only about 18% at a dose level of 0.075 MD-dpa. From Figs. 4(a) and 4(b), along with the results in Fig. 3 for a perfect SiC crystal, it can be seen that the effects of internal strain relaxation increases with increasing dose, such that the reduction in C_{44}, for instance, increases from 14% in a perfect crystal to 63% at the dose of 0.2 MD-dpa. As described previously, a large number of defects are produced during cascade overlap, and the populations of interstitials and vacancies in-
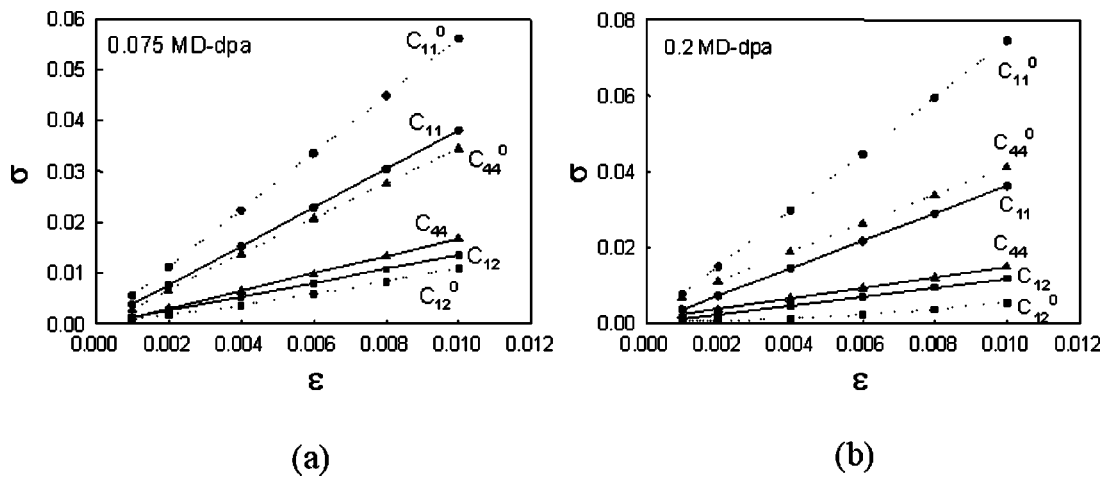
FIG. 4. Stress-strain curves for elastic calculations in the damaged SiC at doses of (a) 0.075 and (b) 0.2 MD-dpa, where the dotted lines represent those obtained without the internal strain relaxation and the solid lines indicate those calculated with full internal strain relaxation.

crease with increasing dose. The increase is slow at low-dose levels, but it has been observed that enhanced defect production due to cascade overlap leads to a faster increase in interstitials and vacancies. Among these defects, it is likely that some defects and defect clusters are formed in metastable configurations that can relax to minimum energy states under applied strains. The increase in the number of these metastable defects with increasing dose can influence the internal strain relaxations. As described above, short-term annealing (about 50 ps) at 200 K has been performed, which may relax some metastable defects into stable configurations. Also, short-term annealing guarantees that the net force on each atom vanishes, but defects and defect clusters can introduce significant local strains in the crystal. To completely remove these metastable configurations, longer-time annealing at higher temperatures is required, which is beyond the scope of the present investigation. It is emphasized that the symmetry breakup due to defects and defect clusters during continued cascade overlap gives rise to significant internal strain relaxations. However, the present results have clearly demonstrated that the internal strain relaxations have significant effects on the calculation of elastic constants in a damaged crystal.

The values of elastic constants can be easily determined from the slopes of the curves in Figs. 3 and 4, as indicated by Eq. (3), and the results are shown in Fig. 5 as a function of dose. The experimental elastic constants for a perfect SiC at room temperature are shown as crosses in the figure, but no direct experimental data for elastic constants in damaged SiC at different dose levels are available. For the dose range studied in the present paper, all elastic constants show expected softening behavior under irradiation. The values for C_{11} and C_{12} continuously decrease with increasing dose, but C_{44} exhibits a certain degree of fluctuation at both low- and high-dose levels. As described above, a large number of metastable point defects and clusters are created during cascade overlap, and these defects should relax to minimum energy states under isotropic and monoaxial expansion, but may not relax to the most stable configurations under the shear applied to calculate C_{44}. In general, the elastic constants de-

crease rapidly at doses less than 0.1 MD-dpa, and the decrease is smaller at the higher dose levels, which suggests that the different defect types that are accumulated at different dose levels may play different roles in the observed behavior of the elastic constants. The analysis of defect accumulation due to cascade overlap[11] has shown that the damage state is dominated by point defects and small cluster at low-dose levels, and their concentration increases sigmoidally with increasing dose. These defects and defect clusters are homogeneously distributed in the MD cell prior to significant amorphization, and induce large distortions of the lattice. The coalescence and growth of these clusters at intermediate and higher doses lead to the formation of amorphous domains and eventually complete amorphization in SiC. These results indicate that point defects and small clusters contribute more significantly to the changes of elastic constants than the topological disorder associated with the highly disorderd or amorphous domains. However, the detailed contribution of the respective numbers of point defects, defect clusters, and amorphous domains to elastic constants cannot be determined because there is not yet a suitable method to define small amorphous clusters in the MD simulations. A topologi-
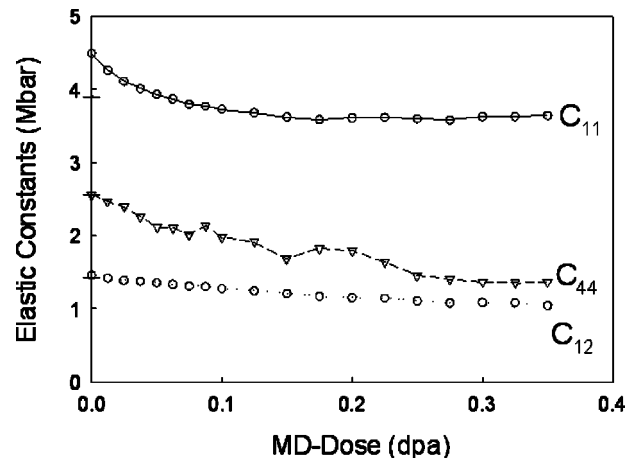

FIG. 5. Variation of elastic constants C_{11}, C_{12}, and C_{44} as a function of dose.

cal analysis method to identify atoms comprising the amorphous state due to cascade overlap events is currently under development,[25] which may clarify the relative contributions to the elastic constants. Similar behavior has been observed in the volume swelling due to damage accumulation,[12] where the isolated defects contribute significantly to the overall swelling of the residual crystalline material during the early stages of damage accumulation. Furthermore, the damage states characterized using long-range order (LRO) and short-range order (SRO) parameters have shown that the LRO parameter decreases continuously with increasing dose until full loss of the LRO occurs once the crystalline-to-amorphization (c-a) transition is complete; however, even at the dose for completion of the c-a transition, some short-range order still remains. The rapid decrease in the SRO parameter occurs at doses less than 0.1 MD-dpa, and further reduction is very small at higher doses. These results, along with the fact that the SRO parameter saturates at about 0.49 after the c-a transition occurs, indicate that a local tetrahedral network exists in the partially and completely amorphized SiC. The similar behavior of the elastic constants and the SRO parameter may suggest that the local tetrahedral network inhibits further decrease of the elastic constants at intermediate and high doses, even if the defect concentration at these dose levels is much higher than that at low doses.

Brillouin scattering techniques have been applied by Okamoto and co-workers[26–28] to study the elastic behavior of Nb_3Ir and Zr_3Al irradiated with ions. The experimental results have shown that elastic softening occurs prior to amorphization in Nb_3Ir and Zr_3Al, and a dramatic reduction in the average shear elastic constant, of up to 40% and 50%, is observed for Nb_3Ir and Zr_3Al, respectively. When disordering is nearly complete in these intermetallic compounds, anomalies in the long-range order parameter, in the sound velocity, and in the lattice parameter reveal that a first-order phase transition occurs to a state characterized by the same shear elastic constant as the amorphous phase. In an effort to account for differences in amorphization tendency among intermetallic compounds, a generalization of the Lindemann melting criterion has been proposed to explain solid-state amorphization.[29,30] The chemical disorder and the accumulation of Frenkel pairs introduced by exchanging randomly selected atoms and removing atoms at random from their sites into interstitial positions were employed to mimic electron-irradiation-induced amorphization in $NiZr_2$.[30] The variation of the average shear elastic constant, G, with the square of the dispersion in the average nearest-neighbor distance, σ^2, shows that the data for amorphization by the two processes, mentioned above, and for melting $NiZr_2$ lie on the same curve. There is a jump in the value of σ^2 and a corresponding sharp drop in G to about zero just above the melting point, which indicates that the liquid state is reached. On the other hand, once the system is amorphized by irradiation, further introduction of defects does not appreciably change σ^2 and G. These results suggest that the variation of the average elastic constant with displacement is similar for all three processes, which is consistent with the generalized Lindamann melting criterion. The present results in SiC are generally consistent with these previous studies in intermetallic compounds. From Fig. 5, it is clearly seen that elastic soft-
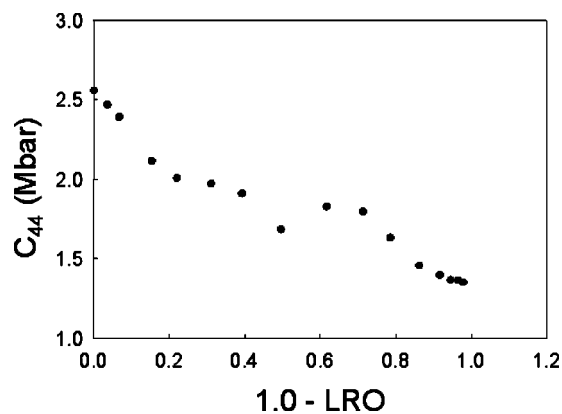

FIG. 6. The shear elastic constant C_{44} as a function of long-range order parameter ($\eta=1.0$-LRO), where $\eta=0$ describes the completely ordered state of SiC, whereas $\eta=1$ expresses the completely disordered state associated with random occupancy of sites.

ening occurs prior to amorphization, and there exists a dramatic reduction in the shear elastic constant of up to 30%. After the c-a transition is complete at 0.28 MD-dpa, the change of the shear elastic constant is very small. In an effort to verify the generalized Lindemann melting criterion, the variation of C_{44} with long-range order (LRO) parameter is calculated and shown in Fig. 6, since the LRO, together with short-range order parameter (SRO), provides direct evidence of ordering, disordering, and amorphization of alloys under irradiation. It is of interest to note that once SiC is amorphized by cascade overlap (LRO ~ 0.08), further overlap events do not appreciably change the C_{44} and LRO parameters. Moreover, the variation of the shear elastic constant with the LRO parameter is generally similar to that obtained in intermetallic compounds, and, therefore, provides support for the generalized Lindemann melting criterion.

Using Eqs. (4), (7), and (8), the bulk modulus, B, and averaged elastic modulus, E, are calculated as a function of dose, and the results are summarized in Fig. 7, where the crosses are experimental data for perfect and amorphous SiC. The elastic modulus represents the mean values of the Reuss and Voigt averages. The changes in bulk and elastic moduli
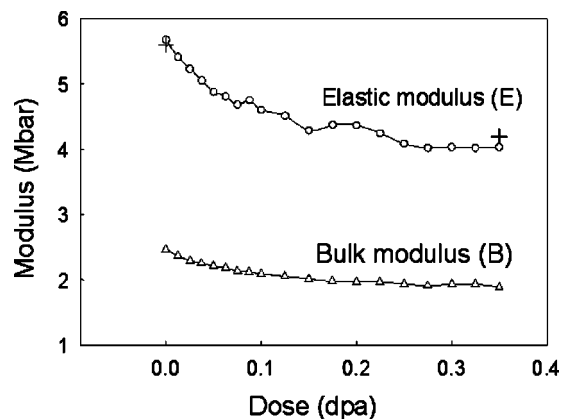

FIG. 7. Variation of elastic modulus, E, and bulk modulus, B, as a function of dose, together with some experimental data (Refs. 7 and 24) for comparison.

TABLE II. Summary of the mechanical properties in the CA-SiC, along with availably experimental data for comparison.

	Present work	Expt.[7]
C_{11}(GPa)	364($\pm$4.36)	—
C_{12}(GPa)	104($\pm$2.72)	—
C_{44}(GPa)	136($\pm$8.44)	—
B(GPa)	189	—
E(GPa)	403	418

show similar behavior to the elastic constants (Fig. 4). In general, these physical properties decrease with increasing dose, exhibiting a reduction of about 23% and 29% for bulk and elastic moduli at the highest dose, respectively. A rapid decrease is observed at low-dose levels, similar to the elastic constants, which is associated with the creation of point defects and small clusters. The effect of the topological disorder on bulk and elastic moduli is small. It is interesting to note that both E and B saturate at 0.28 MD-dpa, indicating no further decrease in the bulk and elastic moduli of the system at higher doses. A previous study[11] has shown that this dose corresponds to completion of the crystalline-to-amorphization transition observed during cascade overlap, which suggests that further irradiation does not significantly alter the mechanical properties of amorphous SiC. The experimental observations by Bolse et al.[31] and Wendler et al.[32] have demonstrated that a correlated tetrahedral network exists in irradiation-induced amorphous SiC, and the local tetrahedral structure is found to be much less disordered compared to other materials.[33] These correlated tetrahedral networks might inhibit further decreases of the bulk and elastic moduli once the fully amorphous state is attained. Only after irradiation to significantly higher doses than that for complete amorphization is a large fraction of the Si-C tetrahedral network in SiC destroyed.

C. Elastic properties in amorphous SiC

The analysis of system energy,[12] order parameters, and topological features[11] have indicated that SiC becomes completely amorphous when the irradiation dose reaches about 0.28 MD-dpa. During further cascade overlap events, large atomic rearrangements take place without increasing the chemical and topological disorder, indicating that a similar local structure remains. Elastic constants, bulk and elastic moduli of the CA-SiC are shown in Table II, along with available experimental data[7] for comparison. In general, C_{ij}, B, and E in the CA-SiC are smaller than those in a perfect crystal, particularly for C_{44}, which is an order of magnitude smaller than that in perfect SiC. The elastic constants in the CA-SiC decrease about 19%, 29%, and 46% for C_{11}, C_{12}, and C_{44}, respectively, and 23% for the bulk modulus and 29% for the elastic modulus. High defect concentration in the CA-SiC, which breaks up the long-range ordered structure, may have a significant effect on the softening of the elastic properties. Statistically, these results suggest that the elastic properties in the CA-SiC appear to be fairly insensi-
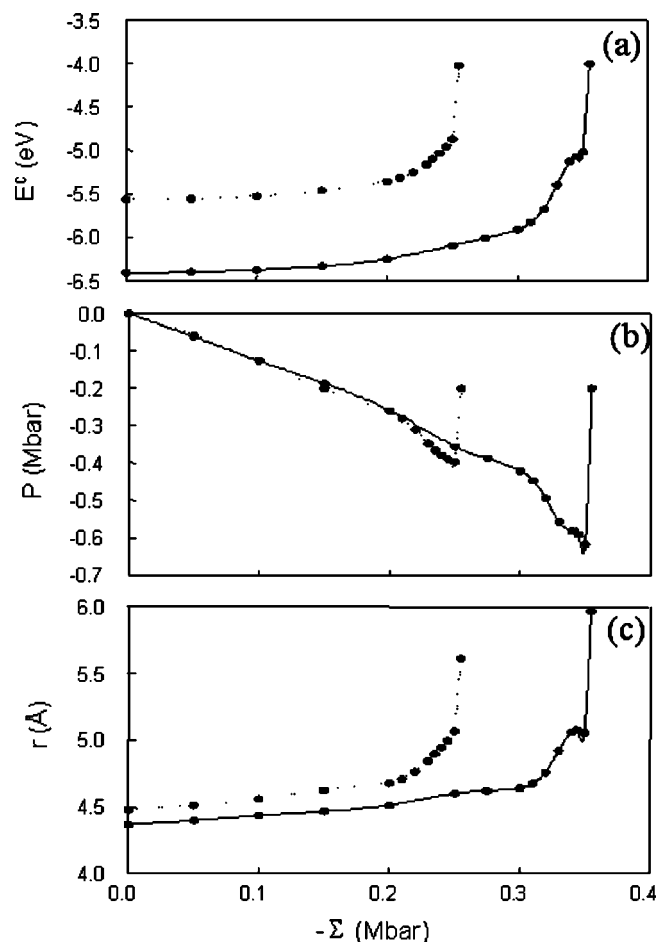

FIG. 8. The simulated structural responses of perfect SiC (solid line) and CA-SiC (dotted line) to applied hydrostatic tension at 300 K. The data for potential energy, internal stress and lattice parameter are averaged over 10 000 time steps except for the last point where the system becomes unstable and continues to change in time.

tive to the defect types and configurations, but sensitive to local tetrahedral network structures. In the case of a completely amorphous material, the elastic properties should be isotropic, and there are only two independent elastic constants, which follow a relation given by

$$C_{44} = \frac{1}{2}(C_{11} - C_{12}). \qquad (8)$$

The calculated elastic constants in Table II give a result that is within 4.6% of satisfying of this relation. The finite size and periodic boundary conditions imposed on the MD cell may prohibit the ideal isotropic structure from forming for the CA-SiC. Weber et al.[7] have measured the hardness and elastic modulus of ion-irradiated 6H-SiC using a Berkovich nanoindenter, and found that the elastic modulus decreases with increasing dose, exhibiting a decrease of 24% for the amorphous state of 6H-SiC (from 550 to 418 GPa). The elastic modulus of neutron-amorphized 6H-SiC measured by Snead et al.[8] also showed a decrease from 528 to 292 GPa.
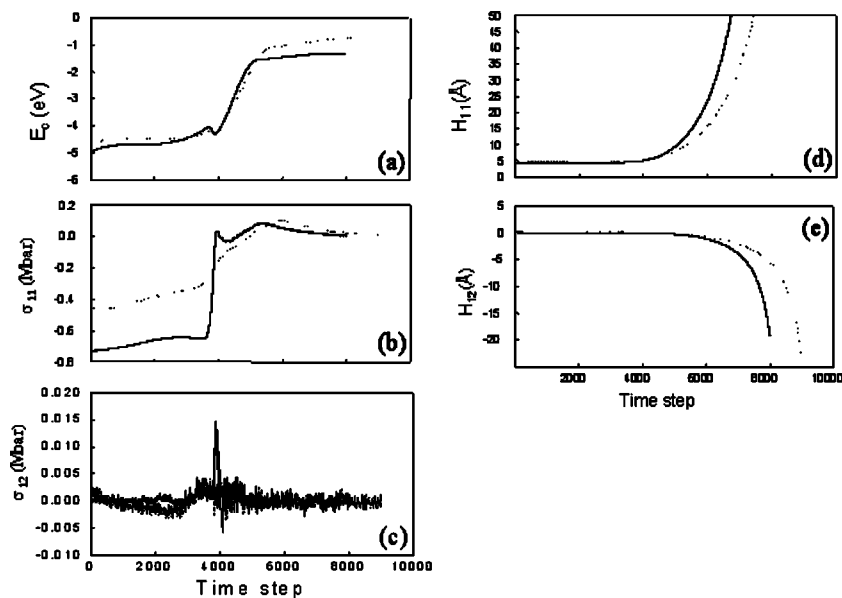
FIG. 9. Time dependence of the systems at the critical hydrostatic stress in perfect SiC (solid lines) and CA-SiC (dotted lines): (a) variation of potential energy, (b) a diagonal element of stress tensor, σ_{11}, and (c) an off-diagonal element of stress tensor, σ_{12}, (d) a diagonal element of cell matrix, H_{11}, and (e) a off-diagonal element of cell matrix, H_{12}.

The present results are in good agreement with these experimental values obtained for 6*H*-SiC.

D. Stability of perfect and cascade-amorphized SiC

Crystal stability under hydrostatic stress is a fundamental problem in elasticity[34] because it represents the critical condition at which the crystal becomes structural unstable, particularly under the conditions of large deformation. While the critical stress can be predicted by stability analysis based on elastic stiffness coefficients,[35] atomistic simulations provide not only a direct observation of crystal behavior under hydrostatic loading, but also new insights into the dynamics processes occurring during structural responses. In order to study the structural stability of the perfect SiC and the CA-SiC, a homogeneous stress, Σ, was applied to the system using the method of Parrinello and Rahman.[36] Initially, the atoms were allowed to equilibrate for about 5 ps for each external loading at 300 K, where a constant temperature was maintained by coupling the atoms in the boundary planes to a heat reservoir, and the physical properties (i.e., potential energy, lattice parameter, and internal pressure) were then determined over 10 000 time steps. Simulations were carried out covering the range of Σ from 0.0 to 0.35 Mbar, with incremental steps of 0.05 at low loading levels, but decreasing to 0.005 when approaching the critical value.

Results for the potential energy per atom, E_c, internal pressure, P, and lattice parameter, r, are shown in Fig. 8 as a function of applied loading, where the solid and dotted lines represent those in perfect SiC and CA-SiC, respectively. It should be noted that the internal pressure includes only the contribution from the potential because stress fluctuation terms require equilibrating the MD cells for much longer times than 5000 steps. However, it is believed that the current simulations essentially capture the general behavior of the system. While potential energy and lattice parameter increase with increased applied loading, the pressure decreases with increased loading for both perfect SiC and CA-SiC. The instability exhibits itself as an unexpected release in internal pressure, increase in potential energy, and increase in lattice parameter, which suggests that a significant structural change has taken place in both the perfect SiC and the CA-SiC. In a perfect SiC crystal, the system is stable at the step where the applied hydrostatic stress is equal to 0.35 Mbar, and all the properties of interest do not vary significantly with time after equilibration. Increases in applied loading to 0.355 Mbar leads the system to be unstable, as indicated by the last data point in Fig. 8, and the properties show no signs of convergence at the end of simulation period (about 15 000 time steps). The observed critical loading at which the structure becomes unstable lies between 0.35 and 0.355 Mbar for the perfect SiC crystal. All properties in the CA-SiC exhibit behavior similar to that for the perfect SiC, as shown in Fig. 8, but the critical loading for CA-SiC to become unstable is much smaller than that for the perfect SiC and lies between 0.25 and 0.255 Mbar. As demonstrated previously, the long-range order is completely lost in the CA-SiC, but the short-range order partially remains, which indicates the existence of some tetrahedral networks. These local networks may respond similar to crystalline SiC, up to some dose, under applied loading.

More details in the nature of the time-dependent system responses to applied loading at $\Sigma = 0.255$ and 0.355 Mbar are provided in Fig. 9 for the CA-SiC and perfect SiC, respectively. The variation of the energies is illustrated in Fig. 9(a), where the solid line represents the time dependence for the perfect SiC, while the dotted line shows that for the CA-SiC. The continuous increase in the energy at early stages suggests that the system is undergoing continuous dilatation for both the perfect SiC and CA-SiC, but an observed decrease occurs at about step 3700 for the perfect SiC, which corresponds to a sharp rise in the diagonal and off-diagonal elements of stress tensor, as shown in Figs. 9(b) and 9(c). The sharp increase in off-diagonal element of the stress tensor, σ_{12}, indicates an early stage of the shear deformation in the perfect SiC, and the subsequent release in off-diagonal elements of the stress tensor reveals that the system has undergone a significant shear deformation. However, the slightly

different behavior of the stress tensor, particularly in the shear stress, can be seen in Figs. 9(b) and 9(c) for the CA-SiC. A detailed analysis of the CA-SiC at zero loading shows that a small shear deformation has been introduced by cascade overlap, and this may illustrate that there is no threshold shear stress needed to initiate shear deformation in the CA-SiC, as observed in the perfect SiC. The slow increase of the σ_{12} in the CA-SiC at about step 2340 clearly indicates that shear deformation due to the applied loading occurs. Also shown in Fig. 9(d) and 9(e) are the variation of a diagonal element, H_{11}, and a off-diagonal element, H_{12}, of the simulation cell as a function of time, where the dimension of the MD cell is expressed in terms of the elements of the cell matrix $\tilde{H}$ (see Ref. 29), with each element representing the edge of the simulation cell. The changes in the simulation cell show similar behavior for both the perfect SiC and CA-SiC. It can be seen that there are two regions, an initial period when the cell maintains its cubic shape with small dilatation, and a second period at about step 4000 when the cell undergoes volume expansion and shear deformation, leading to instability and symmetry breakup of the system, which is consistent with the abrupt change of the σ_{11} shown in Fig. 9(b).

IV. SUMMARY

The microstructural changes in SiC during ion implantation and under neutron irradiation can lead to significant changes in its mechanical properties that affect the performance of SiC-based electronic devices and nuclear components. Using molecular dynamics methods, previously archived files of simulated damage states associated with defect accumulation and disordering due to cascade overlap have been used to investigate the variation of the elastic constants and both the bulk and elastic moduli as a function of dose. The internal strain relaxations have no effect on C_{11} and C_{12} due to the lattice symmetry in a perfect SiC crystal, similar to results reported by others,[19] but the elastic constants obtained by internal strain relaxations in the damaged SiC are significantly different from those without the internal strain relaxations, particular for C_{44}. This is likely due to metastable defects that form during cascade overlap, but which subsequently relax into more stable configurations under applied strains. The calculated elastic constants and the bulk and elastic moduli generally decrease with increasing dose, but the change begins to saturate at doses greater than 0.1 MD-dpa, which suggests that point defects and small clusters may contribute more significantly to the changes of elastic constants than the topological disorder associated with amorphization. When SiC becomes completely amorphous, the elastic constants decrease by about 19%, 29%, and 46% for C_{11}, C_{12}, and C_{44}, respectively. The calculated 29% reduction in the elastic modulus of the CA-SiC is in good agreement with experimental observations that indicate a decrease of 24% for the amorphous state of $6H$-SiC.[7,32]

Molecular dynamics method has been also employed to study the stability of both the perfect SiC and CA-SiC under hydrostatic tension conditions. The potential energy and lattice dilation increase with increased applied loading, whereas, the internal pressure decreases with applied loading for both the perfect SiC and CA-SiC. A significant structural change takes place with the abrupt release of internal pressure and the increases in potential energy, volume expansion, and shear deformation. The critical loading at which the structure becomes unstable lies between 0.35 and 0.355 Mbar for perfect SiC and between 0.25 and 0.255 Mbar for CA-SiC. The local tetrahedral networks that appear to exist in CA-SiC may respond to the observed structural stability under hydrostatic tension.

*Email address: fei.gao@pnl.gov

[1] J. B. Casady and R. W. Johnson, Solid-State Electron. **39**, 1409 (1996).

[2] W. Bolse, Nucl. Instrum. Methods Phys. Res. B **148**, 83 (1999).

[3] K. Minato, K. Sawa, K. Koya, T. Tomita, A. Ishikawa, C. A. Baldwin, W. A. Gabbard, and C. M. Malone, Nucl. Technol. **131**, 36 (2000).

[4] J. A. Lake, R. G. Bennett, and J. F. Kotek, Sci. Am. **286**, 73 (2002).

[5] M. A. Capano and R. J. Trew, MRS Bull. **22**, 19 (1997).

[6] L. L. Snead, D. Steiner, and S. J. Zinkle, J. Nucl. Mater. **191-194**, 566 (1992).

[7] W. J. Weber, L. M. Wang, N. Yu, and N. J. Hess, Mater. Sci. Eng., A **253**, 62 (1998).

[8] L. L. Snead, S. J. Zinkle, J. C. Hay, and M. C. Osborne, Nucl. Instrum. Methods Phys. Res. B **141**, 123 (1998).

[9] C. J. Mchargue, D. L. Joslin, and J. M. Williams, Nucl. Instrum. Methods Phys. Res. B **46**, 185 (1990).

[10] W. J. Weber, N. Yu, L. M. Wang, and N. J. Hess, J. Nucl. Mater. **224**, 258 (1997).

[11] F. Gao and W. J. Weber, Phys. Rev. B **66**, 024106 (2002).

[12] F. Gao and W. J. Weber, J. Mater. Res. **18**, 1877 (2003).

[13] L. Malerba and J. M. Perlado, Phys. Rev. B **65**, 045202 (2002).

[14] Z. Li and R. C. Bradt, Int. J. High Technol. Ceram. **4**, 1 (1988).

[15] F. Gao and W. J. Weber, Phys. Rev. B **63**, 054101 (2000).

[16] F. R. S. Hearmon, *An Introduction to Applied Anisotropic Elasticity* (Oxford University Press, London, 1961).

[17] W. R. L. Lambrecht, B. Segall, M. Methfessel, and M. van Schilfgaard, Phys. Rev. B **44**, 3685 (1991).

[18] R. Devanathan, W. J. Weber, and T. Diaz de la Rubia, Nucl. Instrum. Methods Phys. Res. B **141**, 118 (1998).

[19] M. Tang and S. Yip, J. Appl. Phys. **76**, 2719 (1994).

[20] R. Devanathan and W. J. Weber, J. Nucl. Mater. **278**, 258 (2000).

[21] F. Gao, E. J. Bylaska, W. J. Weber, and L. R. Corrales, Phys. Rev.

B **64**, 245208 (2001).

[22] R. Devanathan, W. J. Weber and F. Gao, J. Appl. Phys. **90**, 2303 (2001).

[23] C. S. G. Cousins, J. Phys. C **11**, 4867 (1978).

[24] D. W. Feldman, J. H. Parker Jr., J. W. Choyke, and L. Patrick, Phys. Rev. **173**, 787 (1968).

[25] X. Yuan, F. Gao, L. W. Hobbs, and W. J. Weber (unpublished).

[26] P. R. Okamoto, L. E. Rehn, J. Pearson, R. Bhadra, and M. Grimsditch, J. Less-Common Met. **140**, 231 (1988).

[27] L. E. Rehn, P. R. Okamoto, J. Pearson, R. Bhadra, and M. Grimsditch, Phys. Rev. Lett. **59**, 2987 (1987).

[28] M. Grimsditch, K. E. Gray, R. Bhadra, R. T. Kampwirth, and L. E. Rehn, Phys. Rev. B **35**, 883 (1987).

[29] N. Q. Lam, P. R. Okamoto, R. Devanathan, and M. Meshii, *Statics and Dynamics of Alloy Phase Transformations*, edited by P. E. A. Turchi and A. Gonis (Plenum, New York, 1994), p. 691.

[30] R. Devanathan, N. Q. Lam, P. R. Okamoto, and M. Meshii, Phys.

Rev. B **48**, 42 (1993).

[31] W. Bolse, J. Conrad, F. Harbsmeier, M. Borowski, and T. Rodle, in *Complex Fluids*, edited by D. Weitz *et al.*, MRS Symposia Proceedings No. 248 (Materials Research Society, Pittsburgh, 1997), p. 319.

[32] E. Wendler, A. Heft, U. Zammit, E. Glaser, M. Marinelli, and W. Wesch, Nucl. Instrum. Methods Phys. Res. B **116**, 398 (1996).

[33] W. J. Weber, R. C. Ewing, C. R. A. Catlow, T. Diaz de la Rubia, L. W. Hobbs, C. Kinoshita, Hj. Matzke, A. T. Motta, M. Nastasi, E. K. H. Salje, E. R. Vance, and S. J. Zinkel, J. Mater. Res. **13**, 1434 (1998).

[34] L. Landau and E. M. Lifshitz, *Theory of Elasticity* (Pergamon, New York, 1986), p. 83.

[35] J. Wang, S. Yip, S. R. Phillpot, and D. Wolf, Phys. Rev. Lett. **71**, 4182 (1993).

[36] M. Parrinello and A. Rahman, J. Appl. Phys. **52**, 7182 (1981).